Thermomechanical modelling of lithospheric slab tearing and its topographic response in the Gibraltar Arc (westernmost Mediterranean Sea)

Kittiphon Boonma[1,2], Daniel Garcia-Castellanos[1], Ivone Jiménez-Munt[1], Taras Gerya[3]

[1] GeoSciences Barcelona, Geo3BCN-CSIC, Lluís Solé i Sabaris, s/n, 08028 Barcelona, Spain

[2] Departament de Dinàmica de la Terra i de l'Oceà, Universitat de Barcelona, Spain

[3] Department of Geophysics, EDRW, ETH Zürich

Correspondence author: Kittiphon Boonma (kittiphon.b@gmail.com)

Key points:

- An oblique initial passive margin (relative to the trench axis) promotes the initiation of a one-sided slab tearing.
- Slab tearing can occur purely from the negative buoyancy force of the subducted slab – the overriding plate dictates very little.
- Slab tearing produced surface uplift-rate of 0.23–2.16 mm/yr, which is consistent with the first stage of the Messinian Salinity Crisis.

Abstract

Lithospheric slab breakoff can occur in various styles including a horizontal ‘tearing’, where an initial weakness develops into tearing and laterally propagates along the slab. Slab tearing has been invoked to explain changes in plate kinematics in the Western Mediterranean and the tectonic uplift that led to the Messinian Salinity Crisis. However, this process remains debated regarding its surface signature and the physical parameters controlling its initiation and dynamics. Here, we use 3D thermo-mechanical modelling to investigate geodynamic parameters affecting the slab-tearing initiation and its lateral propagation, and to quantify the corresponding surface vertical motions. We find that an oblique convergence introduces an asymmetry that favors the initiation of one-sided slab tearing. The tectonic configuration of the overriding plate has little effect on the trench migration rate, and slab tearing can results purely from the negative buoyancy of the subducted slab. This force and the slab retreat it causes are enough to generate an arcuate plan-view shape to the orogen. The slab-tear propagation rate varies from 37–67 cm/yr. During propagation, the slab tearing depth increases along the subducting slab, with a shallow initial tear (80–150 km) and a deeper tear (170–200 km) on the opposite end. The time needed for the slab to detach completely is geologically fast (< 2 Myr). The slab tearing can cause a prominent surface uplift of 0.5–1.5 km throughout the forearc region with an uplift rate of 0.23–2.16 mm/yr, which is consistent with the situation during the first stage of the Messinian Salinity Crisis.

1. Introduction

The perception that large regions of continental crust have risen at rates that cannot be explained by crustal thickening alone, has led to the necessity to identify the mechanism responsible for such rapid surface uplift (England and Molnar, 1990). Slab breakoff is among

the deep-seated mechanisms invoked to justify the long-wavelength, high rates of surface uplift (Davies and von Blanckenburg, 1995). It is driven by the same force that drives slab pull and subduction, i.e., a positive contrast of the potential density of the lithospheric slab relative to the mantle (e.g. Boonma et al., 2019; Garcia-Castellanos et al., 2000; Jiménez-Munt et al., 2019). Slab breakoff is a process happening at depth within the mantle consisting of the detachment of a subducted oceanic lithospheric slab from the more buoyant continental lithosphere during a continental collision. The concept of slab breakoff was first used to explain post-collisional magmatism and exhumation of high-pressure rocks in the European Alps (Davies and von Blanckenburg, 1995). Garzanti et al. (2018), and references therein, gave a comprehensive global overview of where slab breakoff has been invoked to explain changes in plate kinematics and tectonic deformation, e.g. the Alps (Fox et al., 2015; Davies and von Blanckenburg, 1995; Sinclair, 1997), the Mediterranean region (Carminati et al., 1998; Wortel and Spakman, 2000; Rosenbaum et al., 2008; van Hinsbergen et al., 2010), the Anatolia-Zagros orogen (Şengör et al., 2003; Faccenna et al., 2006), and Himalaya and Tibet (van Hinsbergen et al., 2012; Wu et al., 2014; Liang et al., 2016). These studies often ascribe short-lived, long-wavelength exhumation events or sudden pulses in sediment supply to slab breakoff. However, they often neglect the influence of the 3D geometrical configuration of each tectonic regions. How likely was the tectonic configuration in those domains to have caused the slab tearing in the first place? How much does slab breakoff contribute to the buoyancy-driven isostatic surface uplift?

The Western Mediterranean underwent subduction, slab fragmentation, and rollback, under intense crustal deformation including simultaneous N-S compression and E-W extension. Seismic tomography studies (Spakman and Wortel, 2004; Faccenna and Becker, 2010; Garcia-Castellanos and Villaseñor, 2011; Bezada et al., 2013; Bonnin et al., 2014;

Villaseñor et al., 2015; Civiero et al., 2019) indicate that the entire western Mediterranean region overlies structurally complex remnants of subducted lithosphere including fragments of oceanic Tethyan lithosphere inherited from the Mesozoic extension between Eurasia and Africa.

The geodynamics of the Alboran domain are severely debated in all tectonic reconstructions of the Western Mediterranean. In the last decade, nevertheless, most authors point toward subduction rollback (35 Ma) as the key geodynamic process that drives the tectonic evolution of the Western Mediterranean. The disagreements among the proposed models lie in how this rollback couples with tectonic evolution. The main three proposed rollback scenarios are: (i) rollback originates from a long N-NW dipping subduction zone stretching from the Baleares in the north-east to Gibraltar in the west margin (Rosenbaum et al., 2002; Spakman and Wortel, 2004; Van Hinsbergen et al., 2014); (ii) rollback originates from a laterally restricted NW dipping slab confined to the Baleares (Faccenna et al., 2004; Jolivet et al., 2009); or (iii) rollback originates from a SE dipping subduction under the north-African margin (Vergés and Fernàndez, 2012). The major extension of the Alboran domain ended during the middle Miocene (~16 Ma) (e.g. Vergés and Fernàndez, 2012). The distribution of volcanic rocks during the active volcanism period in the Alboran basin has been interpreted as a result of either: (i) the rollback and steepening of a remnant of oceanic slab causing mantle delamination (Duggen et al., 2004, 2008); or (ii) the lateral tearing of the subducting Ligurian-Tethys lithosphere (Wortel and Spakman, 2000) which could have caused the lithospheric thermal thinning.

Based on seismic tomographic imaging, Wortel and Spakman (2000) suggested that slab tearing might have occurred in the Gibraltar Arc region as a consequence of the continental collision and the subsequent slab rollback declined during early Miocene. The majority of topographic growth in the Betics appear to have initiated after late Tortonian (~7 Ma), sometimes under little amounts of tectonic fault deformation (Garcia-Castellanos and Villaseñor, 2011). The vertical movements (uplift) observed in the Internal Betic zone after late Tortonian are best constrained from the present elevation of tectonically undeformed Miocene marine sediment in that region, often above 600 m elevation. This has been interpreted as the result of a westward migration of a lateral tear within the steeply hanging Ligurian-Tethys slab seen in tomography (Garcia-Castellanos and Villaseñor, 2011). However, the timing of this mechanism has been poorly constrained and barely tested by thermo-mechanical models, prompting questions regarding the timing of the tearing initiation and the duration of the tearing process.

The uplift of the intramountain basins within the Betics and Rif (Fig 1) has been linked to the closure of the Gibraltar marine gateways during the Late Miocene which led to the partial desiccation of the Mediterranean Sea, known as the Messinian Salinity Crisis event (Coulson et al., 2019; Garcia-Castellanos and Villaseñor, 2011). The Messinian Salinity Crisis (MSC) (5.96–5.33 Ma) marks a period of dramatic sea-level change, possibly the most abrupt environmental change on Earth since the beginning of the Tertiary.

This study utilises 3D thermo-mechanical modelling to better the understanding of the lithospheric slab tearing process and its consequent surface vertical motions, using the Western Mediterranean as a reference scenario. Firstly, we investigate how different

subduction/collision scenarios and model physical parameters act on the initiation of the slab tearing and its propagation along the trench. Secondly, we quantify the resulting surface elevation changes, which are robustly coupled with the deep geodynamic processes (viscous flow, temperature evolution, and dynamic topography). Lastly, we provide insights into how the slab tearing dynamics fit within the realm of the Western Mediterranean, and how these surface vertical motions help constraining the Messinian Salinity Crisis event.

2. Method

2.1. Numerical method

The modelling in this project was carried out using a 3D thermo-mechanical coupled numerical code, 'I3ELVIS' (Gerya, 2013). The code is based on finite-differences and marker-in-cell numerical schemes (Gerya and Yuen, 2003; Harlow and Welch, 1965). The governing physical laws such as conservation of mass, conservation of momentum, and heat equation are discretised on a staggered Eulerian grid, assuming an incompressible medium (i.e.$\nabla \cdot \vec{v} = 0$). For each time step, fourth order Runge-Kutta scheme spatially advects the markers. The multi-grid method is used to speed up the convergence of the Gauss-Seidel iterative solver.

The rocks' densities vary with temperature T (K) and pressure P (Pa) according to the equation of state:

$$\rho_{P,T} = \rho_0[1 - \alpha(T - T_0)][1 + \beta(P - P_0)], \quad (1)$$

where ρ_0 is the reference density at P_0 = 1 MPa and T_0 = 298.15 K, the coefficient of thermal expansion α = 2×10^{-5} 1/K, and the coefficient of thermal compressibility β = 6×10^{-12} 1/Pa.

Our models take phase transition of olivine in the mantle into account. As the dry olivine is subjected to greater pressure at depths, it first undergoes exothermic phase transition (~ 410 km) and transforms into wadsleyite (Katsura and Ito, 1989). At a greater depth and pressure, the wadsleyite exothermically transforms into ringwoodite (~ 520 km), which decompose (endothermically) into bridgmanite (silicate perovskite) at an even greater depth (~ 660 km) (Ito et al., 1990). The eclogitization of the subducted oceanic crust (basaltic and gabbroic) is taken into account by linearly increasing the density of the crust with pressure from 0% to 16% in the P-T region between the experimentally determined garnet-in and plagioclase-out phase transitions in basalt (Ito and Kennedy, 1971).

2.2. Rheology

The composite visco-plastic (VP) rheology is used with no elasticity. The ductile rheology is approximated by a combination of effective viscosities for diffusion η_{diff} and dislocation η_{disl} creep to compute the ductile rheology $\eta_{ductile}$:

$$1/\eta_{ductile} = 1/\eta_{diff} + 1/\eta_{disl} \quad (2)$$

In the crust, we assume constant grain size and η_{diff} and η_{disl} is computed as:

$$\eta_{diff} = \frac{A}{2\sigma_{cr}^{(n-1)}} exp\left(\frac{E + PV}{RT}\right) \quad (3)$$

$$\eta_{disl} = \frac{A^{1/n}}{2} exp\left(\frac{E + PV}{nRT}\right) \dot{\varepsilon}_{II}^{(1-n)/n} \quad (4)$$

where R is gas constant (8.314 J/(K·mol)), P is pressure (Pa), T is temperature (K), $\dot{\varepsilon}_{II} = \sqrt{1/2(\dot{\varepsilon}_{ij})^2}$ is the the second invariant deviatoric strain-rate tensor, σ_{cr} is the critical stess (assumed diffusion-dislocation transition stress), A is the experimentally determined pre-exponential factor ($Pa^n \cdot s$), E denotes activation energy (J/mol), V is activation volume (J/Pa), and n is the stress exponent of the viscous creep.

In the mantle, the ductile creep is implemented with grain size growth and reduction processes (assisted by Zenner pinning). In the case of the mantle, the composite rheology in

$$\eta_{diff} = \frac{1}{2} A_{diff}\, h^m exp\left(\frac{E_{diff} + PV_{diff}}{RT}\right) \quad (5)$$

$$\eta_{disl} = \frac{1}{2} A_{disl}^{\frac{1}{n}} exp\left(\frac{E_{disl} + PV_{disl}}{nRT}\right) \dot{\varepsilon}_{II}^{(1-n)/n} \quad (6)$$

Eq. 2 still stand where

where, A_{diff} is the experimentally determined pre-exponential factor for diffusion creep (Pa·s) and A_{disl} is pre-exponential factor for dislocation creep (Pa^n·s), *h* is grain size (m), *m* is the grain size exponent. The interplay between diffusion and dislocation creep is controlled by a grain-size evolution equation dependent on the mechanical work and temperature.

The ductile rheology is combined with a brittle rheology to compute an effective visco-plastic

$$\eta_{ductile} \leq \frac{C + \mu P}{2\dot{\varepsilon}_{II}} \quad (7)$$

$$\mu = \begin{cases} \mu_0 - \gamma\mu_\gamma, & \gamma \leq \gamma_0 \\ \mu_1 & , \gamma > \gamma_0 \end{cases} \quad (8)$$

$$\gamma = \int \sqrt{\frac{1}{2}\dot{\varepsilon}_{ij(plastic)}^2}\, dt \quad (9)$$

rheology using the upper limit for ductile viscosity:

where μ is the internal friction coefficient (μ_0 and μ_1 are the initial and final internal friction coefficient, respectively), $\mu_\gamma = (\mu_0 - \mu_1)/\gamma_0$ is the rate of faults weakening with integrated

plastic strain γ (γ_0 is the upper strain limit for the fracture-related weakening), C is the rock compressive strength at $P = 0$, t is time (s), $\dot{\varepsilon}_{ij(\mathrm{plastic})}$ is the plastic strain rate tensor.

2.3. Model setup

The continental collision is modelled with an incoming continental block (Africa), overriding a subducting oceanic plate which is connected to a stationary continental block (Iberia) through a passive margin. The 3D model domain (Fig 2) measures 1500 km × 780 km × 1200 km, with a resolved grid resolution of 4.6 km× 3.0 km × 4.6 km, in the x, y (vertical), and z directions, respectively. The 40-km thick continental crust splits into the upper (20 km) and lower (20 km) continental crust, and thinning toward the ocean. The 8-km thick oceanic crust also splits into the upper (basaltic, 3 km) and lower (gabbroic, 5 km) oceanic crust. Partial melting and melt extraction processes are neglected in our simplified models.

The initial adiabatic temperature gradient (0.5°C/km) is prescribed in the asthenospheric mantle. The continental geotherm is prescribed as a linear variation from the model surface (0°C, 273 K) to the lithosphere-asthenosphere boundary (1344°C, 1617 K) at 110 km depth. The initial thermal structure of the oceanic lithosphere is calculated using the half-space cooling model (e.g. Turcotte and Schubert, 2014) based on a slab age of 110 Ma and a thermal diffusivity of 10^{-6} m^2/s. The thermal boundary in the lower boundary of the model is prescribed as the infinite-like external constant temperature, which is implemented by $\partial T/\partial z = (T_{external} - T)/\Delta z_{external}$, where $T_{external}$ is 1707°C (1980 K) at 1080 km depth at the bottom external boundary (outside the model box), and $\Delta z_{external}$ is the vertical distance between the bottom of the model box and the bottom external boundary where $T = T_{external}$, in this case $\Delta z_{external}$ = 300 km.

The velocity boundary conditions are free slip on all sides except the bottom boundary, which is permeable in both upward and downward directions. This permeable bottom boundary is prescribed as an infinite-like external free slip conditions at 1080 km depth. The external free slip permits the global mass conservation in the computational domain and is implemented as $\partial v_x/\partial z = 0, \partial v_z/\partial z = -v_z/\Delta z_{external}$, where $\Delta z_{external}$ is the vertical distance between the bottom of the model box and the bottom external boundary where the free slip condition ($\partial v_x/\partial z = 0, v_z = 0$) is satisfied, in this case $\Delta z_{external}$ = 300 km.

The elevation of the lithosphere is calculated dynamically as an internal free surface through a 22 km thick layer of 'sticky air' (η_{air} = 10^{18} Pa·s, ρ_{air} = 1 kg/m^3) on top of the continental plate and 25 km on top of the oceanic plate (Gerya, 2010). We implemented a simplified erosion condition in our model, where instantaneous sedimentation limits a trench depth to 8 km below the water level and the instantaneous erosion is prescribed at 8 km above the initial continental crustal surface where rock markers change into sticky-air markers.

All of the experiments are two-stage experiments. The first stage is a period of forced convergence (rate of 47 mm/yr) until the subducted slab reaches 200 km depth. We prescribed the initial convergence at x=1386 km within the two transform fault weak-zones, labelled 'ridge' in Fig 2c. The initial convergence rate is purposely fast in order to create a sufficient hanging slab with minimised thermal diffusion. After the first stage, the obtained thermo-mechanical state is used as an initial setup for continental collision. In the second stage, the prescribed convergence rate is either removed, so that the slab sinks due to its own

weight (Mod1-reference, Mod2, Mod3, and Mod4), or reduced to a lower value of 4 mm/yr, resembling the convergence rate in the Western Mediterranean (Mod5).

3. Results

All the numerical experiments were performed using 24 cores on the ETH-Zürich EULER cluster. Note that all model times 't' (in Myr) are given from the initiation of stage 2 for each model.

3.1. Reference model (Mod1-reference)

After the slab has reached the depth of 200 km, the prescribed convergence rate stopped. As the dense slab continues to sink under its own weight (Table 1), the Iberian continental margin started to bend downward and the incoming African block overrides the passive margin. At t=3.84–4.10 Myr, the lithospheric thinning/necking started on the slab's easternmost side (z=800 km) at 120 km depth (Fig 3c). Immediately after the detachment, at 4.24 Myr, the incoming continental block (Africa) came to a complete stop, which, in turn, causes a change in the slab's downward velocity. The slab's portion in the vicinity of the tearing appear to have lowered downward velocity, which means the attached portion of the slab continues to sink with a faster downward velocity (Fig 3c, d). The tearing point propagates westward reflecting in the tilted angle of the slab's top edge as shown in the Fig 3e and Fig 4.

While the slab is fully attached, the down-dip motion of the slab induced corner flows, and the large slab body induced a large flow around the slab's edges (Fig 5). The slab's

easternmost part is the only region in which the continental-continental collision occurs which leads to slab tearing (Fig 4a1). Any previously present oceanic crust in the forearc wedge appears to have been removed by the thermal erosion. Once the tearing caused the incoming Africa block to stop completely, the tear propagates westward. As you look westward, the subsequent tearing now is a result of the tearing process that has been set in motion from the east, and not a tearing due to continental-continental collision. The different amount of exhumed oceanic crust in the forearc wedge (Fig 4b2,c3) appear to be depending on how large the remaining oceanic domain is in between the incoming African plate and the Iberian plate. We observe a larger amount of exhumed oceanic crust in the westernmost side (Fig 4c3).

This initiation of slab tearing is observable as a sharp surface uplift along the collisional belt, with uplift rate ranges from 0.23 mm/yr to 2.16 mm/yr throughout the tear propagation. The rise in elevation (Fig 4a, b, c) also evolves westward, reflecting the tear propagation occurring deeper in the mantle. The tearing occurs due to great stress in the bending zone created by both the buoyancy of the Iberia block (upward force) and the weight of the hanging slab (downward force). The slab is completely detached after t=5.75 Myr (tearing duration of ~1.65 Myr).

3.2. Influence of model parameters

3.2.1. Effect of no incoming continental block (Mod2)

The reference model (Mod1-reference) had an incoming buoyant continental block implemented to create a continental-continental collision, which then led to a one-sided slab tearing. We now move on to look at how the lack of this incoming buoyant continental block

would affect the subduction zone dynamic. Rheologically, Mod2 mimics Mod1-reference but the absence of an incoming continental block creates a continental-oceanic arc. At t=3.48 Myr, the retreating intra-oceanic subduction trench reaches the continental passive margin, after which the trench continues to retreat. After 0.5 Myr, high topography developed over the trench (Supplementary Fig S1a). Here on the eastern side of the slab, the accumulation of crustal materials above the trench prevented the trench from retreating any further and led to the initiation of slab tearing at t=4.66 Myr. The slab is completely detached by t=5.70 Myr (tearing duration of ~1.04 Myr). The uplift rate during the tear propagation ranges from 0.71 mm/yr to 1.35 mm/yr. The lack of incoming continental block thus does not prevent the initiation of slab tearing.

In Mod2, where the overriding plate does not have a buoyant continental block, the slab-tearing dynamics are similar to the Mod1-reference, likely since both models have the same mantle rheological setup. Mod2's lack of a buoyant continental block on the overriding plate does not appear to hinder the rate of trench retreat that is thus mainly controlled by the oceanic slab buoyancy and asthenospheric mantle viscosity. In Mod1-reference, the presence of an incoming buoyant continental block does limit the extent of the forearc region, as illustrated in Fig 6. A less dense body (relative to the surrounding mantle) rises up the subduction channel and thrusts under the overlying crustal materials (Fig 6c, e, and f). The lighter mantle pushed-up crustal material then spread over the forearc region at the surface. The absence of a continental block in Mod2 allows the crustal material to spread farther compared to Mod1-reference, where the spreading is limited by the buoyant continental block.

3.2.2. Effect of a higher ductile viscosity of the mantle (Mod3)

The subduction in the reference model is spontaneous i.e. the slab falls by its own weight resulting in the subsequent trench retreat. However, the slab sinks with a velocity far greater than what we would expect in the Western Mediterranean region. Another model was constructed with a more viscous mantle, which can be achieved by increasing the ductile viscosity through increasing the activation volume of the mantle (both V_{diff} and V_{disl}), in the hope of slowing down the down-going slab due to the increased resistance of the higher-viscosity sublithospheric mantle. In the model Mod1-reference, the activation volume for the dislocation creep was V_{disl}=2.6 J/(mol·MPa) and for diffusion creep V_{diff}=0.7 J/(mol·MPa), and in this model Mod3, V_{disl}=3.0 J/(mol·MPa) and V_{diff}=0.8 J/(mol·MPa) (Table 1). The increased activation volume means the stronger mantle viscosity increase with pressure (and therefore with depth). The evolution of the subduction is similar to the reference model but with much slower rate. For example, when the slab has reached 450 km depth, the slab in Mod1-reference has a maximum downward velocity of 20 cm/yr (t=3.05 Myr) where as Mod3's maximum downward velocity is 8 cm/yr (t=6.87 Myr). The slab tearing in Mod3 initiated at around t=11.08 Myr as oppose to t=4.34 Myr in the reference model. The surface topography above the initiation of tearing exhibits an elevation of ~1.5 km (Supplementary Fig S2d), which is similar to Mod1-reference. The uplift rate during the tear propagation ranges from 0.75 mm/yr to 1.68 mm/yr. In Mod3, the slab tear initiated at t=9.80 Myr and the slab completely detached by t=12.95 Myr (tearing duration of ~1.87 Myr).

The less viscous mantle in the reference model allows the slab to sink down with ease, which resulted in the trench retreat at the rate of 20 cm/yr. The more viscous mantle in Mod3 offers higher resistance for the down-going slab and results in the trench retreat rate of 10 cm/yr. The fast down-going slab, together with the fast trench retreat velocity in the reference

316 model, causes segments of high stress (4–5 MPa) and high strain-rate (10^{-14}–10^{-12} 1/s) to
317 develop at the depth of greater than 120 km which led to a deeper breakoff depth. In Mod3,
318 with more viscous mantle, the down-going slab is better supported by the surrounding
319 asthenosphere leading to a more gradual and shallow stress build-up focussing within the
320 bending zone of the slab. This shallow stress focussing, at the depth of less than 100 km, led
321 to a shallower breakoff compared to the reference model.

322

323 **3.2.3. Effect of higher brittle strength of the mantle (Mod4)**

324 Another way to increase the viscosity of the mantle is to increase the brittle viscosity, i.e. the
325 upper limit of the visco-plastic viscosity. Similar to Mod3, the increased mantle viscosity in
326 Mod4 aims to slow down the sinking slab such that we can study the characteristics of slab
327 tearing, which evolved too quickly between modelling time-steps in Mod1-reference. In
328 Mod4 model, we increased final internal friction coefficient (μ_1 in Eq. (8) for the lower
329 oceanic crust and the mantle, from zero in Mod1-reference to 0.3 in Mod4 (Table 1). By
330 increasing this coefficient value: (1) we decrease the rate of strain weakening by a factor of
331 two; and (2) we significantly increase the effective visco-plastic viscosity of deformed cold
332 lithospheric mantle at elevated pressures/depths. After the initial push, the slab failed to sink
333 down into the asthenosphere on its own due to a high resistance to local brittle/plastic
334 deformation associated with the slab retreat and bending. This lack of slab's downward
335 velocity also led to the termination of trench retreat altogether (Supplementary Fig S3a and
336 d). The slab only reached 300 km in depth and hang there with the angle of the hanging slab
337 slightly steepened. The lack of trench retreat means the incoming continental block (Africa)
338 did not reach the passive margin (Iberia) and so there is no collision and no slab tearing. This

rheological setup with strong brittle/plastic- mantle, therefore, does not favour the slab tearing.

3.2.4. Effect of fixed the convergence velocity (Mod5)

In model Mod5, after the initial push and the slab has reached the depth (y) of 200 km, the velocity is reduced to 4 mm/yr to mimic the average convergent velocity between the Iberian and African plates (Macchiavelli et al., 2017). This velocity is much slower than the velocity resulting from the hanging slab in previous runs, so this change should slow down the slab retreat. Such slow velocity exposes the hanging slab to a fast thermal diffusion in the surrounding asthenosphere. No slab tearing occurs in this model, but instead a lithospheric dripping takes place (Supplementary Fig S4).

Lithospheric delamination needs a velocity that is fast enough for thermal advection to prevail over thermal diffusion and maintain the internal temperature of the slab and its higher density (Boonma et al., 2019). However, the low convergent velocity in our region of study (4 mm/yr) causes the slab to experience a greater degree of thermal diffusion than thermal advection and, therefore, could not maintain its low internal temperature and high density, all of which led to thermal erosion and lithospheric dripping (Supplementary Fig S4). The great amount of thermal diffusion that the slab experienced and the amount of time that the slab is hanging in the sublithospheric mantle allow an arcuate (in plan-view) deformed lower-viscosity slab to develop. In the models with spontaneous subduction (Mod1-reference, Mod2, Mod3, and Mod4), the subduction and trench migration comes to a stop once the slab reached the passive margin and the tear has started. In Mod5, however, the continuous

pushing of the incoming continental block creates a band of high elevation over the arcuate trench (Supplementary Fig S4d).

4. Discussion

4.1. Geometry of the passive margin and the slab-tearing dynamics.

In our experiments, the continental passive margin makes an oblique angle with the trench such that the incoming subduction zone arrives first at the easternmost side (z=800 km in Fig 2c). In all of the models that developed slab tearing (Mod1-reference, Mod2, and Mod3), the tear initiated on the easternmost side (z=800 km), and the tearing point *T* then propagates westward (toward z=0 km). Averaging over a 500-km distance, the tear velocities approximately are 42.6 cm/yr in Mod1-reference, 67.6 cm/yr in Mod2, and 37.6 cm/yr in Mod3 (Table 2). Our tear-propagation rates fall well within the range of previous estimations: 7–45 cm/yr from the Carpathians' depocenter migration by Meulenkamp et al. (1996); and 10–80 cm/yr from 3D numerical modelling of continental collision by van Hunen and Allen (2011). A theoretical calculation based on 3D stress model by Yoshioka and Wortel (1995) even showed a tear propagation rate as low as 2–4 cm/yr.

Overall, the slab takes less than 2 Myr to completely detach (over the entire slab length of 600–700 km), which is fast in a geological timescale (compared to the timescales needed for subduction). The factor that seems to have some control over the timing of the tearing is the mantle rheology. The more viscous mantle in Mod3 slowed down the sinking slab, hence the slowest tear-propagating velocity.

385 The tearing depth, with the oblique configuration of the continental passive margin, varies
386 along the subduction zone. On the easternmost side, where the tear initiated, the tearing depth
387 is shallow (~80–150 km) as the tear is caused by the weakness in the transition zone between
388 the continental and the oceanic lithosphere. While on the western side the tearing depth is
389 deeper (~170–200 km) as the tear, here, is not only caused by the tectonic variation of the
390 transition zone but also (i) the negative buoyancy of the hanging and detached portion of the
391 slab and (ii) the high velocity mantle influx in the slab tear window (Fig 5). The range of
392 breakoff depths from our models falls within similar range as previous numerical modelling
393 studies: 80–240 km from Freeburn et al. (2017), 95–140 km from Schellart (2017), 100–400
394 km from Gerya et al. (2004), and 120–145 km from Duretz et al. (2014). A similar pattern is
395 reflected in the breakoff location. On the easternmost side, the breakoff tends to occur within
396 the subducted continental lithosphere portion, such that the detached slab pinched out some
397 continental crust. Since the westward side the slab tear depth is deeper, therefore, the
398 breakoff tends to be within the subducted oceanic lithosphere portion.

399

400 The derived reconstruction of several geological settings, such as Carpathian Mountains
401 (Meulenkamp et al., 1996; Wortel, 2000; Göğüş et al., 2016), the Banda Arc (Spakman and
402 Hall, 2010), the Aegean (Jolivet et al., 2013), and the Western Mediterranean (Vergés and
403 Fernàndez, 2012), show the presence of non-straight passive margins. Our simplified models
404 that exhibits slab tearing (Mod1-reference, Mod2, and Mod3) highlight how the orientation of
405 the passive margin dictates the detachment style. A 3D numerical model of slab breakoff by
406 van Hunen and Allen (2011) exhibits a ‘slab-window’ where the slab detachment occur in the
407 centre of the slab then propagate outwards to both edges. However, with our oblique
408 continental passive margin (subducting plate), the subduction zone arrives at the margin at
409 different time along the passive margin. This, in turn, dictates where the one-sided slab

tearing initiates. The easternmost side of the subduction zone arrived at the passive margin first. The arrival of the trench at the transition between continental and oceanic lithosphere exert high stress onto the bending zone of the subducting slab, together with the toroidal flow around the slab's edge, lead to necking and eventually initiate the tearing on the eastern side.

In free-subduction settings (models Mod1-reference, Mod2, Med3, and Mod4), the oblique nature of the passive margin also leads to different trench geometry along the subduction zone. As the trench comes to a stop once it reached the passive margin and the slab started to tear, this means that the gap between the trench and the passive margin would be larger toward the west (e.g. Fig 6). Therefore, the accretionary wedge on the eastern side (toward z=800 km) would be smaller than on the western side (toward z=0 km), where there is larger gap allowing more exhumed crustal material to resurface (Fig 6).

Mode5, with the convergence velocity fixed to 4 mm/yr, is the only model that had developed an arcuate orogen and slab. However, the arcuate slab observed in Mod5 is not as bent as the slab structure interpreted from seismic tomography beneath the Gibraltar Arc System (e.g. Spakman and Wortel, 2004; Bezada et al., 2013). It takes roughly 100 Myr after the continental collision to form ~600 km long arcuate orogen on the surface. We learn that the arcuate slab and orogen can develop through a combination of events: (1) *sufficiently slow convergence rate* – to prevent the formation of a large hanging slab, which could potentially lead to slab tearing; (2) *continuous convergence* – slab tearing will cause the convergence to stop in the case of a spontaneous subduction but a continuous convergence will keep the subduction and continental collision going and causes an arcuate slab and orogen to develop, as in Mod5. The constant convergence velocity was pushing the continental collision with

evenly distributed far-field tectonic force (through model's grid system); this gave rise to the symmetrically arcuate slab observed in Mod5 (Supplementary Fig S**4**). However, seismic tomographic interpretations have shown that the slab beneath the Gibraltar Arc System is of asymmetrical nature with a greater degree of curvature to the west than what we observed in Mod5. Such great degree of slab arcing could illustrate that, during its evolution, the convergence velocity must had been varied along the length of the subduction zone that created the hanging Rif-Gibraltar-Betics (RGB) slab; or multi-directional tectonic forces could have been at play as well (e.g. plate reconstruction of Iberian and NW African plate by Macchiavelli et al. (2017).

4.2. Surface uplift

4.2.1. Dynamic topography

There are two components which are thought to be shaping the surface topography we observed today, the crustal isostatic compensation effect and dynamic topography (Forte et al., 1993). Dynamic topography is caused by the buoyancy-driven mantle convection exerting vertical stress onto the lithosphere. Dynamic subsidence is caused by downward mantle flow (downwelling), while dynamic uplift is caused by upward mantle flow (upwelling). Fig 7 shows model Mod3's evolution of dynamic topography and the corresponding density distribution. We calculated the isostatic effect with a compensation depth of 150 km (~128 km below crustal surface). This isostatic elevation is due to the density changes at crustal and lithosphere scales, without accounting the dynamics of the slab subduction. The dynamic topography then came from taking the isostatic effect away from the modelled elevation. The dynamic uplift is at its peak at t=10.44 Myr (Fig 7a) when the incoming continental crust terminates. While there is mantle downwelling in the mantle wedge (corner flow), the

458 sublithospheric mantle flow upward and, in the process, exhuming the subducted oceanic
459 crustal material up toward the trench. This upward flow and exhumation gave rise to the
460 dynamic uplift which spans over the forearc region (x=350–440 km).

461

462 Once the westward lateral tear has reached our cross-section z=300 km, the upward flow and
463 exhumation in the subduction channel stops (Fig 7c). The mantle flow now focuses on the
464 sinking and detaching slab. The reduction of mantle convection in the sublithosphere reduces
465 dynamic uplift greatly. When the detached slab is a depth of 450–660 km (Fig 7d), the mantle
466 convection cells re-established themselves and returned to the unperturbed pre-detachment
467 stage.

468

469 We also set out to look at the time-response of surface topography to tearing in the mantle
470 and the possible temporal delay involved. The one-to-one (instantaneous) interpretation has
471 been widely utilised by previous studies (Lithgow-Bertelloni and Silver, 1998; Boschi et al.,
472 2010; Faccenna and Becker, 2010; Faccenna et al. 2014; Gvirtzman et al., 2016; Heller and
473 Liu, 2016; Austermann and Forte, 2019; Ávila and Dávila, 2020). Our methodology did not
474 allow resolving any such significant temporal lag between the deep process of tearing and the
475 surface topographic response. This conclusion is based on a time step for the forward
476 modelling of 0.2–0.3 Myr, but the resolution for the time lag is probably large because of the
477 error involved in separating the static and the dynamic components of the vertical isostatic
478 motions. Besides, the tearing in our models occurs at a relatively fast velocity, which may
479 make it difficult to capture and quantify this delay. The dynamic topography shown in Fig 7
480 appears to be reflecting the mantle dynamics well. Prior to slab tearing, the mantle flowing
481 upwards in the subduction channel corresponds with the high dynamic topography (Fig 7a,

b). After tearing has begun, the tearing gap allows the mantle flow to go through and this channel upward flow is reduced (Fig 7c, d).

4.2.2. Uplift signature

Fig 8 displays the modelled evolution of the topographic response as the slab tearing laterally propagates westward. The incoming continental block collided with the passive margin and subsequently came to a complete stop. The initial continental-continental collision (prior to tearing) caused a high topography (~1 km high) on the eastern side (z=800 km) (Fig 8a). As the tear propagates westward, the elevation increases in the same direction (Fig 8b, c, d). The increase in surface elevation does not occur only above the tear position but also in the proximate area, as shown in Fig 8e and 8f that the highest amount of uplift is not necessarily in the same location as the tear. A possible explanation is that as a tear gap opens, it permits a higher density of poloidal flow to flow through, which induces trenchward mantle flow. This rush of poloidal flow then induces a basal drag that drives trenchward motions under the two colliding plates. This trenchward motion exerts compressional force to the relatively immobile subduction zone hinge, in addition to the opposing force from the collision, leading to an uplift of 0.3–0.8 km even before the arrival of the tear (Fig 8e). Jiménez-Munt et al. (2019) estimated similar values of the pulled down topography by the Strait of Gibraltar slab. As the tearing propagates further westward, the high topography on the eastern side starts to subside by as much as 0.2 km (Fig 8e).

As the slab sinks further, its volume in the mantle increases, obstructing the mantle flow and giving rise to corner flow in the mantle wedge. The corner flow increased the velocity of mantle convection (by 3–10 cm/yr, Fig 7a), which gave viscous support to the overlaying

crusts. As slab tearing initiates, it immediately opens up a new channel, which the mantle quickly flow through to replace the volume previously taken up by the slab. This sudden rush of mantle flow could be giving viscous support to the overlying crust (Fig 7a, b, c), which leads to the sudden surface uplift (modelled elevation and isostatic compensation), a prominent signature of slab detachment. The dynamic topography, corresponding to the aforementioned mantle-flow rush, decreases (Fig 7a, b, c) as slab tearing has started on the eastern side (z = 800 km) and thus the exhumation and corner flow is reduced in velocity.

The mantle convection around the detached and sinking slab remains strong at this stage as the slab sinks at such a steep angle that it still obstructs mantle flow (Fig 7c). After the detached slab sinks further down, the bottom of the slab hits the depth of 660–700 km discontinuity and rest there, which causes the slab to begin to sink in a flatter manner (e.g. Fig 3f). As the detach slab lays flatter, the mantle convection velocity reduce (by 3–10 cm/yr), or return to normality (~4 cm/yr), because now there is no large body to obstruct the mantle flow and neither a heavy slab pulling down the mantle. This reduced velocity of mantle convection means there is less mantle dynamics going on, which would reduce the dynamic support that was exerting onto the crust. The crust and the lithospheric mantle begin to readjust, thermally, and the previously uplifted surface (by 0.5–1.0 km) begins to subside. Overall, the surface uplift rates observed in our models, as a response to the slab tearing, range from 0.23–2.16 mm/yr. The predicted surface uplift rates previously quantified by numerical modelling studies range widely as low as 0.10 mm/yr to as high as 2.65 mm/yr (Andrews and Billen, 2009; Duretz et al, 2011).

529 Supplementary Fig S5 shows the stacked time-evolution of surface elevation of the slice from
530 Mod3 at position z=780 km. As the subduction zone was approaching the passive margin, the
531 continental block on the overriding plate exhibit an elevation of ~0.8 km (Supplementary Fig
532 S5a). Once the trench has contacted with the passive margin (at ~9 Myr) and the tearing
533 process has initiated, the accretionary wedge gave rise to a surface elevation of up to 2 km in
534 the forearc area southwards of the trench line (Supplementary Fig S5b). High elevation areas
535 (~2 km) on the continental passive margin also increase as the subduction zone pushed
536 northwards. After a period of slab detachment, 1.9 Myr for Mod3, both the continental block
537 on the overriding plate and the accretionary wedge decrease in topography (after 11.70 Myr,
538 Supplementary Fig S5). The area on the passive margin, northern of the compression zone
539 (x=150–180 km), also start to subside with elevation decreased as much as 0.5 km.

540

541 **4.3. Implications for the Western Mediterranean**

542 The oblique nature of the southern Iberian margin may have played a key role in triggering
543 slab tearing from one end of the slab, similar to our models. Based on a tectonic
544 reconstruction of the Ligurian-Tethys between Iberia and Africa during the Late Cretaceous,
545 Vergés and Fernàndez (2012) proposed that a SE-dipping subducted slab started retreating
546 under the NW African margin and retreated NW-wards to the present-day Gibraltar Arc
547 location (Fig 1). The subduction would imply an initial oblique collision at the margin
548 between Iberia and Africa. Alternatively, looking at the tectonic reconstruction of the same
549 region as proposed by Rosenbaum et al. (2002a), Spakman and Wortel (2004), and Van
550 Hinsbergen et al. (2014), where the initially short subduction started from the Baleares,
551 elongated, split up, and then rotated westward into the Gibraltar Arc System. The portion of
552 the subduction zone that moves into the Gibraltar Arc System would also be on a collision
553 course with the oblique southern Iberian margin. This could potentially lead to the slab

554 tearing from one side as observed in the interpreted seismic tomography of the Western
555 Mediterranean (Spakman and Wortel, 2004).

556

557 The limitation of our models lies in the lack of an arcuate slab so a full comparison cannot be
558 made with the interpreted 3D slab structure beneath the Gibraltar Arc System (Spakman and
559 Wortel, 2004). The uplift of intramountain basins within the Betics in southern Iberia is
560 higher on the eastern side (Iribarren et al., 2009; Garcia-Castellanos and Villaseñor, 2011),
561 where the slab is interpreted to be detached based on seismic tomography (Fig 9b). Such
562 uplift is not detected in the western Betics where the tear point is and the part of the same
563 slab still remains attached (Fig 9a). Our models predict a similar trend, with earlier and
564 higher uplift on the eastern parts of the oblique margin (due to both continental-continental
565 collision and slab tearing), and later and lower uplift in the west, where the slab still remain
566 attached. The study of magnetostratigraphic sequences shows that the transition from marine
567 to continental conditions of intramountain basins within the Betics is younging westward (Fig
568 1) (Garcés et al., 1998; Iribarren et al., 2009). This trend corresponds with our models'
569 westward tear propagation, where the oldest uplifted region would be toward the east and the
570 younger uplifted region toward the west.

571

572 The uplift rates from this work (0.23 mm/yr to 2.16 mm/yr) are consistent with the situation
573 during the first stage of the MSC event, in which the uplift of the seaway is compensated for
574 the erosion of seaway, allowing continous but limited water inflow from the Atlantic into the
575 Mediterranean Sea. The tectonic and erosion model by Garcia-Castellanos and Villaseñor
576 (2011) proposed that a critical uplift rate of 5 mm/yr is needed to close the seaways across the
577 Gibraltar Arc. Coulson et al. (2019) built upon Garcia-Castellanos and Villaseñor (2011)'s

model by incorporating an ice-age sea level theory, which predicts a critical uplift rate of <1.5 mm/yr.

5. Conclusion

We set out to investigate the slab tearing process, its dynamics, and its effect on surface topography using three-dimensional thermomechanical modelling, using the Western Mediterranean as a reference scenario. Our results support the idea that an initial passive margin oblique to the trench axis leads to some along-axis asymmetry of the subduction that in turn promotes the tearing initiation on one end of the subducted slab (the end where the subduction reaches the margin first). We show that the tectonic configuration of the overriding plate (continental: 2700–3000 kg/m^3; oceanic: 3000–3100 kg/m^3) has little effect on the trench migration rate as illustrated by our model Mod2 without incoming continental block. The slab tearing can occur purely from the negative buoyancy force of the subducted slab. This force and the slab retreat it causes are enough to generate an arcuate plan-view shape to the orogen. For our Betic Cordillera-inspired setting, the slab-tear propagation rates vary from ~37.6–67.6 cm/yr, which agree with those predicted from previous studies. The tear propagation rate appears to be controlled by the viscosity of the surrounding mantle (10^{18}–10^{21} Pa·s in our models).

The slab tearing depth increases as it propagates along the slab, with a shallower tear (~80–150 km) on the side where the tear initiated and a deeper tear (~170–200 km) on the other side. The timing of the slab tearing in our models appears to be geologically fast (≤3 Myr). The key controls on the duration of detachment process are the viscosity of the

sublithospheric mantle and the amount of shortening/oceanic subduction prior tearing (this affects how large and heavy the slab would be).

Our models are consistent with surface (topographic) uplift in response to the slab tearing process in the upper mantle. We observed a sharp uplift of 0.5–1.5 km throughout the forearc region throughout the tearing process, and gradually decreased after a complete detachment. The uplift trend from east to west agrees with the ages of the marine sediments observed in the intramountain basins from the Betics. Our study also shows that the uplift rate corresponding to slab tearing is in the range of 0.23–2.16 mm/yr, which is consistent with the uplift rate needed to close the Gibraltar Strait seaways during the first stage of the Messinian Salinity Crisis. The effects of relatively unconstrained parameters such as mantle's viscosity, different lithospheric mantle thicknesses, or convergence rate should be further explored in the future.

6. Acknowledgement

This work has been supported by EU Marie Curie Initial Training Network 'SUBITOP' (674899-SUBITOP-H2020-MSCA-ITN-2015), the Spanish Government national research program (GeoCAM, PGC2018-095154-B-I00) and the Generalitat de Catalunya grant (AGAUR 2017 SGR 847). We thank the Laboratorio de Geodinámica at GEO3BCN-CSIC as well as the Euler Cluster at the Scientific Computing centre at ETH Zürich for providing the computing facilities.

7. Author Contributions Statement

Kittiphon Boonma: Methodology, Software, Investigation, Formal analysis, Validation, Writing – Original Draft, Visualisation. **Daniel Garcia-Castellanos**: Conceptualisation, Resources, Funding acquisition, Supervision, Validation, and Writing – Review & Editing. **Ivone Jiménez-Munt**: Conceptualisation, Resources, Funding acquisition, Supervision, Validation, and Writing – Review & Editing. **Taras Gerya**: Methodology, Software, and Writing – Review & Editing.

8. Data Availability Statement

The 3D numerical modelling code, I3ELVIS (Gerya, 2013) used in this study, which is a version implemented with grain-size reduction, is available from http://doi.org/10.5281/zenodo.4637879. The model setup codes are available from https://osf.io/j7gy6/ (Center for Open Science repository).

9. Declaration of competing interest

The authors declare no competing interests.

10. References

Andrews, E. R., & Billen, M. I. (2009). Rheologic controls on the dynamics of slab detachment. *Tectonophysics*, *464*(1–4), 60–69. https://doi.org/10.1016/j.tecto.2007.09.004

Austermann, J., & Forte, A. M. (2019). The importance of dynamic topography for understanding past sea-level changes. *Past Global Changes Magazine*, *27*(1). https://doi.org/10.22498/pages.27.1.18

Ávila, P., & Dávila, F. M. (2020). Lithospheric thinning and dynamic uplift effects during slab window formation, southern Patagonia. *Journal of Geodynamics*, *133*, 101689. https://doi.org/10.1016/j.jog.2019.101689

Bezada, M. J., Humphreys, E. D., Toomey, D. R., Harnafi, M., Dávila, J. M., & Gallart, J. (2013). Evidence for slab rollback in westernmost Mediterranean from improved upper mantle imaging. *Earth and Planetary Science Letters*, *368*, 51–60. https://doi.org/10.1016/j.epsl.2013.02.024

Bonnin, M., Nolet, G., Villaseñor, A., Gallart, J., & Thomas, C. (2014). Multiple-frequency tomography of the upper mantle beneath the African/Iberian collision zone. *Geophysical Journal International*, *198*(3), 1458–1473. https://doi.org/10.1093/gji/ggu214

Boonma, K., Kumar, A., Garcia-Castellanos, D., Jiménez-Munt, I., & Fernández, M. (2019). Lithospheric mantle buoyancy: the role of tectonic convergence and mantle composition. *Scientific Reports*, *9*(1), 17953. https://doi.org/10.1038/s41598-019-54374-w

Boschi, L., Faccenna, C., & Becker, T. W. (2010). Mantle structure and dynamic topography in the Mediterranean Basin. *Geophysical Research Letters*, *37*(20), 20303. https://doi.org/10.1029/2010GL045001

Carminati, E., Wortel, R., Spakman, W., & Sabadini, R. (1998). The role of slab detachment processes in the opening of the western–central Mediterranean basins: some geological and geophysical evidence. *Earth and Planetary Science Letters*, *160*(3–4), 651–665. https://doi.org/10.1016/S0012-821X(98)00118-6

Civiero, C., Custódio, S., Rawlinson, N., Strak, V., Silveira, G., Arroucau, P., & Corela, C. (2019). Thermal Nature of Mantle Upwellings Below the Ibero-Western Maghreb Region Inferred From Teleseismic Tomography. *Journal of Geophysical Research: Solid Earth*, *124*(2), 1781–1801. https://doi.org/10.1029/2018JB016531

Coulson, S., Pico, T., Austermann, J., Powell, E., Moucha, R., & Mitrovica, J. X. (2019). The role of isostatic adjustment and gravitational effects on the dynamics of the Messinian salinity crisis. *Earth and Planetary Science Letters*, *525*. https://doi.org/10.1016/j.epsl.2019.115760

Davies, J. H., & von Blanckenburg, F. (1995). Slab breakoff: A model of lithosphere detachment and its test in the magmatism and deformation of collisional orogens. *Earth and Planetary Science Letters*, *129*(1–4), 85–102. https://doi.org/10.1016/0012-821X(94)00237-S

Duggen, S., Hoernle, K., Klügel, A., Geldmacher, J., Thirlwall, M., Hauff, F., … Oates, N. (2008). Geochemical zonation of the Miocene Alborán Basin volcanism (westernmost Mediterranean): geodynamic implications. *Contributions to Mineralogy and Petrology*, *156*(5), 577–593. https://doi.org/10.1007/s00410-008-0302-4

Duggen, Svend, Hoernle, K., van den Bogaard, P., & Harris, C. (2004). Magmatic evolution of the Alboran region: The role of subduction in forming the western Mediterranean and causing the Messinian Salinity Crisis. *Earth and Planetary Science Letters*, *218*(1–2), 91–108. https://doi.org/10.1016/S0012-821X(03)00632-0

Duretz, T., Gerya, T. V., & Spakman, W. (2014). Slab detachment in laterally varying subduction zones: 3-D numerical modeling. *Geophysical Research Letters*, *41*(6), 1951–1956. https://doi.org/10.1002/2014GL059472

Duretz, Thibault, Gerya, T. V., & May, D. A. (2011). Numerical modelling of spontaneous slab breakoff and subsequent topographic response. *Tectonophysics*, *502*(1–2), 244–256. https://doi.org/10.1016/j.tecto.2010.05.024

England, P., & Molnar, P. (1990). Surface uplift, uplift of rocks, and exhumation of rocks. *Geology*, *18*(12), 1173–1177. https://doi.org/10.1130/0091-7613(1990)018<1173:SUUORA>2.3.CO;2

683 Faccenna, C., & Becker, T. W. (2010). Shaping mobile belts by small-scale convection. *Nature*, *465*(7298),
684 602–605. https://doi.org/10.1038/nature09064

685 Faccenna, C., Becker, T. W., Miller, M. S., Serpelloni, E., & Willett, S. D. (2014). Isostasy, dynamic
686 topography, and the elevation of the Apennines of Italy. *Earth and Planetary Science Letters*, *407*, 163–
687 174. https://doi.org/10.1016/j.epsl.2014.09.027

688 Faccenna, C., Bellier, O., Martinod, J., Piromallo, C., & Regard, V. (2006). Slab detachment beneath eastern
689 Anatolia: A possible cause for the formation of the North Anatolian fault. *Earth and Planetary Science*
690 *Letters*, *242*(1–2), 85–97. https://doi.org/10.1016/J.EPSL.2005.11.046

691 Faccenna, C., Piromallo, C., Crespo-Blanc, A., Jolivet, L., & Rossetti, F. (2004). Lateral slab deformation and
692 the origin of the western Mediterranean arcs. *Tectonics*, *23*(1), n/a-n/a.
693 https://doi.org/10.1029/2002TC001488

694 Forte, A. M., Peltier, W. R., Dziewonski, A. M., & Woodward, R. L. (1993). Dynamic surface topography: A
695 new interpretation based upon mantle flow models derived from seismic tomography. *Geophysical*
696 *Research Letters*, *20*(3), 225–228. https://doi.org/10.1029/93GL00249

697 Fox, M., Herman, F., Kissling, E., & Willett, S. D. (2015). Rapid exhumation in the Western Alps driven by
698 slab detachment and glacial erosion. *Geology*, *43*(5), 379–382. https://doi.org/10.1130/G36411.1

699 Freeburn, R., Bouilhol, P., Maunder, B., Magni, V., van Hunen, J., Hunen, J. Van, & van Hunen, J. (2017).
700 Numerical models of the magmatic processes induced by slab breakoff. *Earth and Planetary Science*
701 *Letters*, *478*, 203–213. https://doi.org/10.1016/j.epsl.2017.09.008

702 Garcés, M., Krijgsman, W., & Agustí, J. (1998). Chronology of the late Turolian deposits of the Fortuna basin
703 (SE Spain): Implications for the Messinian evolution of the eastern Betics. *Earth and Planetary Science*
704 *Letters*, *163*(1–4), 69–81. https://doi.org/10.1016/S0012-821X(98)00176-9

705 Garcia-Castellanos, D., & Villaseñor, A. (2011). Messinian salinity crisis regulated by competing tectonics and
706 erosion at the Gibraltar arc. *Nature*, *480*(7377), 359–363. https://doi.org/10.1038/nature10651

707 Garcia-Castellanos, Daniel, Torne, M., & Fernàndez, M. (2000). Slab pull effects from a flexural analysis of the
708 Tonga and Kermadec trenches (Pacific Plate). *Geophysical Journal International*, *141*(2), 479–484.
709 https://doi.org/10.1046/j.1365-246X.2000.00096.x

710 Garzanti, E., Radeff, G., & Malusà, M. G. (2018, February 1). Slab breakoff: A critical appraisal of a geological
711 theory as applied in space and time. *Earth-Science Reviews*. Elsevier.
712 https://doi.org/10.1016/j.earscirev.2017.11.012

713 Gerya, T. (2010). *Introduction to Numerical Geodynamic Modelling*.
714 https://doi.org/10.1017/CBO9780511809101

715 Gerya, T., & Yuen, D. (2003). Characteristics-based marker-in-cell method with conservative finite-differences
716 schemes for modeling geological flows with strongly variable transport properties. *Physics of the Earth*
717 *and Planetary Interiors*, *140*(4), 293–318. https://doi.org/10.1016/j.pepi.2003.09.006

718 Gerya, T. V., Yuen, D. A., & Maresch, W. V. (2004). Thermomechanical modelling of slab detachment. *Earth*
719 *and Planetary Science Letters*, *226*(1–2), 101–116. https://doi.org/10.1016/j.epsl.2004.07.022

720 Gerya, T. V. (2013). Three-dimensional thermomechanical modeling of oceanic spreading initiation and
721 evolution. *Physics of the Earth and Planetary Interiors*, *214*, 35–52.
722 https://doi.org/10.1016/j.pepi.2012.10.007

723 Göğüş, O. H., Pysklywec, R. N., & Faccenna, C. (2016). Postcollisional lithospheric evolution of the Southeast
724 Carpathians: Comparison of geodynamical models and observations. *Tectonics*, *35*(5), 1205–1224.
725 https://doi.org/10.1002/2015TC004096

726 Gvirtzman, Z., Faccenna, C., & Becker, T. W. (2016). Isostasy, flexure, and dynamic topography.
727 *Tectonophysics*, *683*, 255–271. https://doi.org/10.1016/j.tecto.2016.05.041

728 Harlow, F. H., & Welch, J. E. (1965). Numerical Calculation of Time-Dependent Viscous Incompressible Flow
729 of Fluid with Free Surface. *Physics of Fluids*, *8*(12), 2182. https://doi.org/10.1063/1.1761178

730 Heller, P. L., & Liu, L. (2016). Dynamic topography and vertical motion of the U.S. Rocky Mountain region

prior to and during the Laramide orogeny. *Bulletin of the Geological Society of America*, *128*(5–6), 973–988. https://doi.org/10.1130/B31431.1

Hirth, G., & Kohlstedt, D. (2003). Rheology of the upper mantle and the mantle wedge: A view from the experimentalists, 83–105. https://doi.org/10.1029/138GM06

Iribarren, L., Vergés, J., & Fernàndez, M. (2009). Sediment supply from the Betic–Rif orogen to basins through Neogene. *Tectonophysics*, *475*(1), 68–84. https://doi.org/10.1016/j.tecto.2008.11.029

Ito, E., Akaogi, M., Topor, L., & Navrotsky, A. (1990). Negative pressure-temperature slopes for reactions forming MgSiO 3 perovskite from calorimetry. *Science*, *249*(4974), 1275–1278. https://doi.org/10.1126/science.249.4974.1275

Ito, K., & Kennedy, G. C. (1971). An Experimental Study of the Basalt-Garnet Granulite-Eclogite Transition. In J. G. Heacock (Ed.), *The Structure and Physical Properties of the Earth's Crust* (Vol. 14, pp. 303–314). American Geophysical Union (AGU). https://doi.org/10.1029/GM014p0303

Jiménez-Munt, I., Torne, M., Fernàndez, M., Vergés, J., Kumar, A., Carballo, A., & García-Castellanos, D. (2019). Deep Seated Density Anomalies Across the Iberia-Africa Plate Boundary and Its Topographic Response. *Journal of Geophysical Research: Solid Earth*, *124*(12), 13310–13332. https://doi.org/10.1029/2019JB018445

Jolivet, L., Faccenna, C., Huet, B., Labrousse, L., Le Pourhiet, L., Lacombe, O., … Driussi, O. (2013). Aegean tectonics: Strain localisation, slab tearing and trench retreat. *Tectonophysics*, *597–598*, 1–33. https://doi.org/10.1016/j.tecto.2012.06.011

Jolivet, L., Faccenna, C., & Piromallo, C. (2009). From mantle to crust: Stretching the Mediterranean. *Earth and Planetary Science Letters*, *285*(1–2), 198–209. https://doi.org/10.1016/J.EPSL.2009.06.017

Karato, S. -i., & Wu, P. (1993). Rheology of the upper mantle: a synthesis. *Science (New York, N.Y.)*, *260*(5109), 771–778. https://doi.org/10.1126/science.260.5109.771

Katsura, T., & Ito, E. (1989). The system Mg 2 SiO 4 -Fe 2 SiO 4 at high pressures and temperatures: Precise determination of stabilities of olivine, modified spinel, and spinel. *Journal of Geophysical Research: Solid Earth*, *94*(B11), 15663–15670. https://doi.org/10.1029/JB094iB11p15663

Liang, X., Chen, Y., Tian, X., Chen, Y. J., Ni, J., Gallegos, A., … Teng, J. (2016). 3D imaging of subducting and fragmenting Indian continental lithosphere beneath southern and central Tibet using body-wave finite-frequency tomography. *Earth and Planetary Science Letters*, *443*, 162–175. https://doi.org/10.1016/J.EPSL.2016.03.029

Lithgow-Bertelloni, C., & Silver, P. G. (1998). Dynamic topography, plate driving forces and the African superswell. *Nature*, *395*(6699), 269–272. https://doi.org/10.1038/26212

Macchiavelli, C., Vergés, J., Schettino, A., Fernàndez, M., Turco, E., Casciello, E., … Tunini, L. (2017). A New Southern North Atlantic Isochron Map: Insights Into the Drift of the Iberian Plate Since the Late Cretaceous. *Journal of Geophysical Research: Solid Earth*, *122*(12), 9603–9626. https://doi.org/10.1002/2017JB014769

Meulenkamp, J. E., Kováč, M., & Cicha, I. (1996). On Late Oligocene to Pliocene depocentre migrations and the evolution of the Carpathian-Pannonian system. *Tectonophysics*, *266*(1–4), 301–317. https://doi.org/10.1016/S0040-1951(96)00195-3

Ranalli, G. (1995). *Rheology of the Earth* (2nd ed.).

Rosenbaum, G., Gasparon, M., Lucente, F. P., Peccerillo, A., & Miller, M. S. M. S. (2008). Kinematics of slab tear faults during subduction segmentation and implications for Italian magmatism. *Tectonics*, *27*(2), n/a-n/a. https://doi.org/10.1029/2007TC002143

Rosenbaum, G., Lister, G. S., & Duboz, C. (2002a). Reconstruction of the tectonic evolution of the western Mediterranean since the Oligocene. *Journal of the Virtual Explorer*, *8*(January). https://doi.org/10.3809/jvirtex.2002.00053

Rosenbaum, G., Lister, G. S., & Duboz, C. (2002b). Relative motions of Africa, Iberia and Europe during Alpine orogeny. *Tectonophysics*, *359*(1–2), 117–129. https://doi.org/10.1016/S0040-1951(02)00442-0

Schellart, W. P. (2017). A geodynamic model of subduction evolution and slab detachment to explain Australian plate acceleration and deceleration during the latest Cretaceous-early Cenozoic. *Lithosphere*, *9*(6), 976–986. https://doi.org/10.1130/L675.1

Şengör, A. M. C., Özeren, S., Genç, T., & Zor, E. (2003). East Anatolian high plateau as a mantle-supported, north-south shortened domal structure. *Geophysical Research Letters*, *30*(24). https://doi.org/10.1029/2003GL017858

Sinclair, H. D. (1997). Flysch to molasse transition in peripheral foreland basins: The role of the passive margin versus slab breakoff. *Geology*, *25*(12), 1123–1126. https://doi.org/10.1130/0091-7613(1997)025<1123:FTMTIP>2.3.CO;2

Spakman, W., & Wortel, R. (2004). A Tomographic View on Western Mediterranean Geodynamics. In *The TRANSMED Atlas. The Mediterranean Region from Crust to Mantle* (pp. 31–52). Berlin, Heidelberg: Springer Berlin Heidelberg. https://doi.org/10.1007/978-3-642-18919-7_2

Spakman, Wim, & Hall, R. (2010). Surface deformation and slab-mantle interaction during Banda arc subduction rollback. *Nature Geoscience*, *3*(8), 562–566. https://doi.org/10.1038/ngeo917

Turcotte, D., & Schubert, G. (2014). *Geodynamics*. Cambridge University Press. https://doi.org/10.1017/CBO9780511843877

Van Hinsbergen, D. J. J. J., Vissers, R. L. M. M., & Spakman, W. (2014). Origin and consequences of western Mediterranean subduction, rollback, and slab segmentation. *Tectonics*, *33*(4), 393–419. https://doi.org/10.1002/2013TC003349

van Hinsbergen, D. J. J., Kaymakci, N., Spakman, W., & Torsvik, T. H. (2010). Reconciling the geological history of western Turkey with plate circuits and mantle tomography. *Earth and Planetary Science Letters*, *297*(3–4), 674–686. https://doi.org/10.1016/J.EPSL.2010.07.024

van Hinsbergen, D. J. J., Lippert, P. C., Dupont-Nivet, G., McQuarrie, N., Doubrovine, P. V, Spakman, W., & Torsvik, T. H. (2012). Greater India Basin hypothesis and a two-stage Cenozoic collision between India and Asia. *Proceedings of the National Academy of Sciences of the United States of America*, *109*(20), 7659–7664. https://doi.org/10.1073/pnas.1117262109

van Hunen, J., & Allen, M. B. (2011). Continental collision and slab break-off: A comparison of 3-D numerical models with observations. *Earth and Planetary Science Letters*, *302*(1–2), 27–37. https://doi.org/10.1016/j.epsl.2010.11.035

Vergés, J., & Fernàndez, M. (2012). Tethys–Atlantic interaction along the Iberia–Africa plate boundary: The Betic–Rif orogenic system. *Tectonophysics*, *579*, 144–172. https://doi.org/10.1016/j.tecto.2012.08.032

Villaseñor, A., Chevrot, S., Harnafi, M., Pazos, A., Serrano, I., Córdoba, D., … Ibarra, P. (2015). Subduction and volcanism in the Iberia–North Africa collision zone from tomographic images of the upper mantle. *Tectonophysics*, *663*, 238–249. https://doi.org/10.1016/J.TECTO.2015.08.042

Wortel, M. J. R. (2000). Subduction and Slab Detachment in the Mediterranean-Carpathian Region. *Science*, *290*(5498), 1910–1917. https://doi.org/10.1126/science.290.5498.1910

Wu, F.-Y., Ji, W.-Q., Wang, J.-G., Liu, C.-Z., Chung, S.-L., & Clift, P. D. (2014). Zircon U-Pb and Hf isotopic constraints on the onset time of India-Asia collision. *American Journal of Science*, *314*(2), 548–579. https://doi.org/10.2475/02.2014.04

Yoshioka, S., & Wortel, R. (1995). Three-dimensional numerical modeling of detachment of subducted lithosphere. *Journal of Geophysical Research*, *100*(B10). https://doi.org/10.1029/94jb01258

11. Tables

Table 1 **Material properties used in the numerical experiments**. The flow law include: A is the pre-exponential factor; E denotes activation energy; V is activation volume; n is the stress exponent; m is grain size exponent; σ_{cr} is critical stress or the the assumed diffusion-dislocation transition stress; C is the rock compressive strength at P=0 MPa; μ_0 and μ_1 are the initial and final internal coefficients, respectively parameters (Karato and Wu, 1993; Ranalli, 1995; Hirth and Kohlstedt, 2003; Turcotte and Schubert, 2014). The subscripts 'diff' and 'disl' indicate that those parameters are associated with diffusion and dislocation creep processes, respectively. Mod3 has higher values for mantle activation volume than other models. Mod4 has higher final internal friction coefficient for lower oceanic crust and the mantle. Other properties for all rock types include: heat capacity C_p = 1000 J/(kg·K), thermal expansion $\alpha = 2 \times 10^{-5}$ 1/K; and compressibility $\beta = 6 \times 10^{-12}$ 1/Pa.

Material	**Density ρ_0 (kg/m^3)**	**Thermal conductivity (W/m·K) at T_K, P_{MPa}**	**Flow Law**	**Flow law parameters**
Upper continental crust (Felsic)	2750	0.64+807/(T+77)	Wet quartzite (Ranalli, 1995)	A =1.97×10^{17} Pa^{n}s, n=2.3, E=1.54×10^5 J/mol, V=0 J/(mol·MPa), σ_{cr}=3×10^4 Pa, C=3 MPa, μ_0=0.3, μ_1=0
Lower continental crust (Gabbro)	3000	1.18+474/(T+77)	Plagioclase An75 (Ranalli, 1995)	A =4.80×10^{22} Pa^{n}s, n=3.2, E=2.38×10^5 J/mol, V=0 J/(mol·MPa), σ_{cr}=3×10^4 Pa, C=3 MPa, μ_0=0.3, μ_1=0
Upper oceanic crust (Basalt)			Wet quartzite (Ranalli, 1995)	A =4.80×10^{22} Pa^{n}s, n=3.2, E=2.38×10^5 J/mol, V=0 J/(mol·MPa), σ_{cr}=3×10^4 Pa, C=3 MPa, μ_0=0, μ_1=0
Lower oceanic crust (Gabbro)			Plagioclase An75 (Ranalli, 1995)	A =4.80×10^{22} Pa^{n}s, n=3.2, E=2.38×10^5 J/mol, V=0 J/(mol·MPa), σ_{cr}=3×10^4 Pa, C=3 MPa, μ_0=0.6, μ_1=0.0 **Mod4**: μ_1=0.3
Mantle	3300	0.73+1293/(T+77) ×exp(0.000004P)	Dry olivine (Hirth & Kohlstedt, 2003)	m=3, A_{diff} =1.50×10^{15} Pa s, E_{diff}=3.75×10^5 J/mol, V_{diff}=0.7 J/(mol·MPa), A_{disl} =1.10×10^{16} Pa^{n}s, n=3.5, E_{disl}=5.30×10^5 J/mol, V_{disl}=2.6 J/(mol·MPa), C=3 MPa, μ_0=0.6, μ_1=0.0 **Mod3**: V_{diff}=0.8 J/(mol·MPa), V_{disl}=3.0 J/(mol·MPa) **Mod4**: μ_1=0.3
Mantle weak zone				m=3, A_{diff} =1.50×10^{15} Pa s, E_{diff}=3.75×10^5 J/mol, V_{diff}=0.7 J/(mol·MPa), A_{disl} =1.10×10^{16} Pa^{n}s, n=3.5, E_{disl}=5.30×10^5 J/mol, V_{disl}=2.6 J/(mol·MPa), C=3 MPa, μ_0=0, μ_1=0

Table 2 **Model list**.

Model	Description	Incoming Continent	Slab detachment	Slab tear propagation (cm/yr)	Tearing duration (Myr)	Uplift rate from tearing (mm/yr)
Mod1	Reference model	Yes	Yes	42.6	1.65	0.23 – 2.16
Mod2	No incoming continental block	No	Yes	67.6	1.04	0.71 – 1.35
Mod3	Higher ductile viscosity of the mantle	Yes	Yes	37.6	1.87	0.75 – 1.68
Mod4	Higher brittle strength of the mantle	Yes	No	-	-	-
Mod5	Fixed the convergence velocity	Yes	No	-	-	-

12. Figures

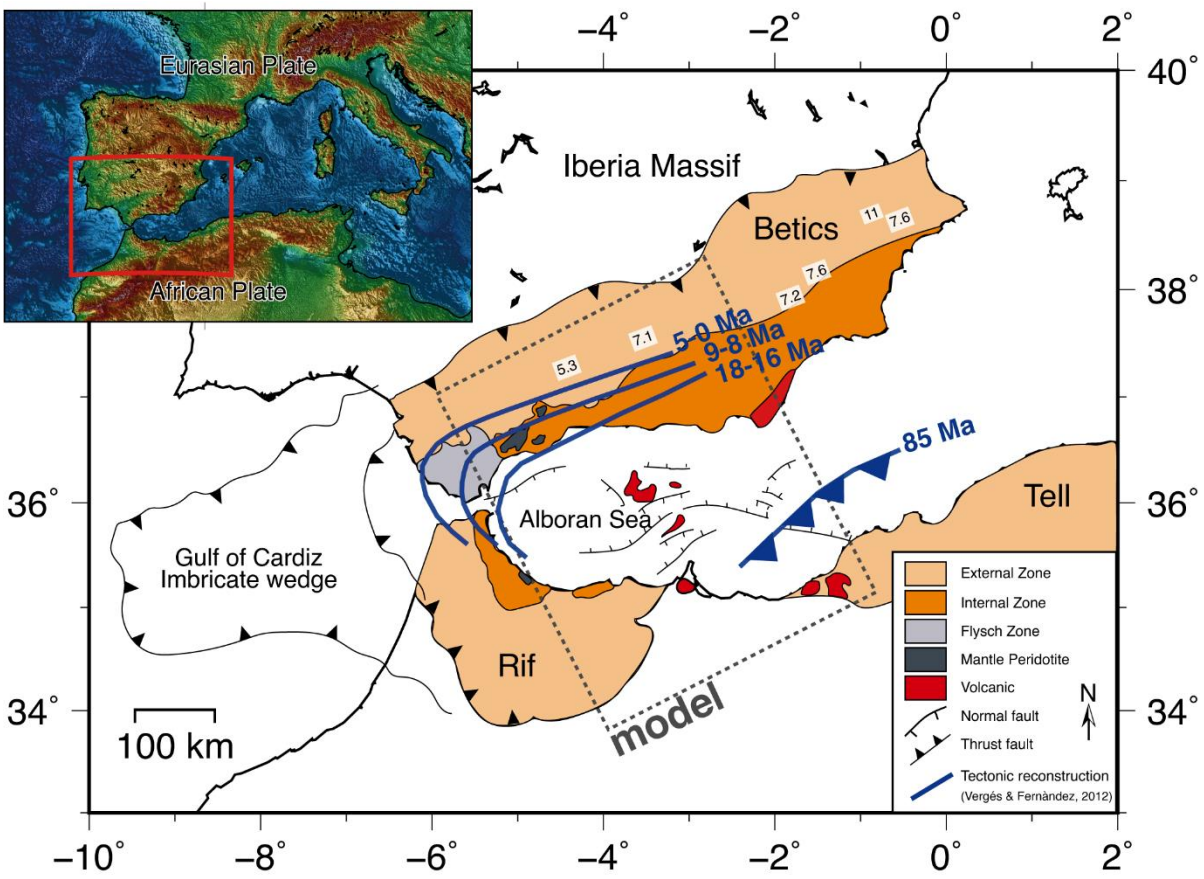

Fig 1. **Gibraltar Arc region**. A present-day schematic map of the Western Mediterranean region, specifically the Gibraltar Arc System (after Rosenbaum et al., 2002a). The inset is a topography-bathymetry map, with our region of interest in the red box. The map displays key units of the Gibraltar Arc System: External Zone, Internal Zone, and the Flysch Zone (Suture Zone). The blue lines are the reconstruction of the Ligurian-Tethys domain between Iberia and Africa (Late Cretaceous) before the onset of the African convergence, as proposed by Vergés and Fernàndez (2012). The grey frame outlines the area and the basic features therein, which the model setup is based on. The model frame is at such angle to encapsulate the stages from the reconstruction that involve slab detachment i.e. from 18–0 Ma. The numbers in white rectangles are the ages in Ma of the transition from marine to continental conditions of intramountain basins within the Betics (Iribarren et al., 2009).

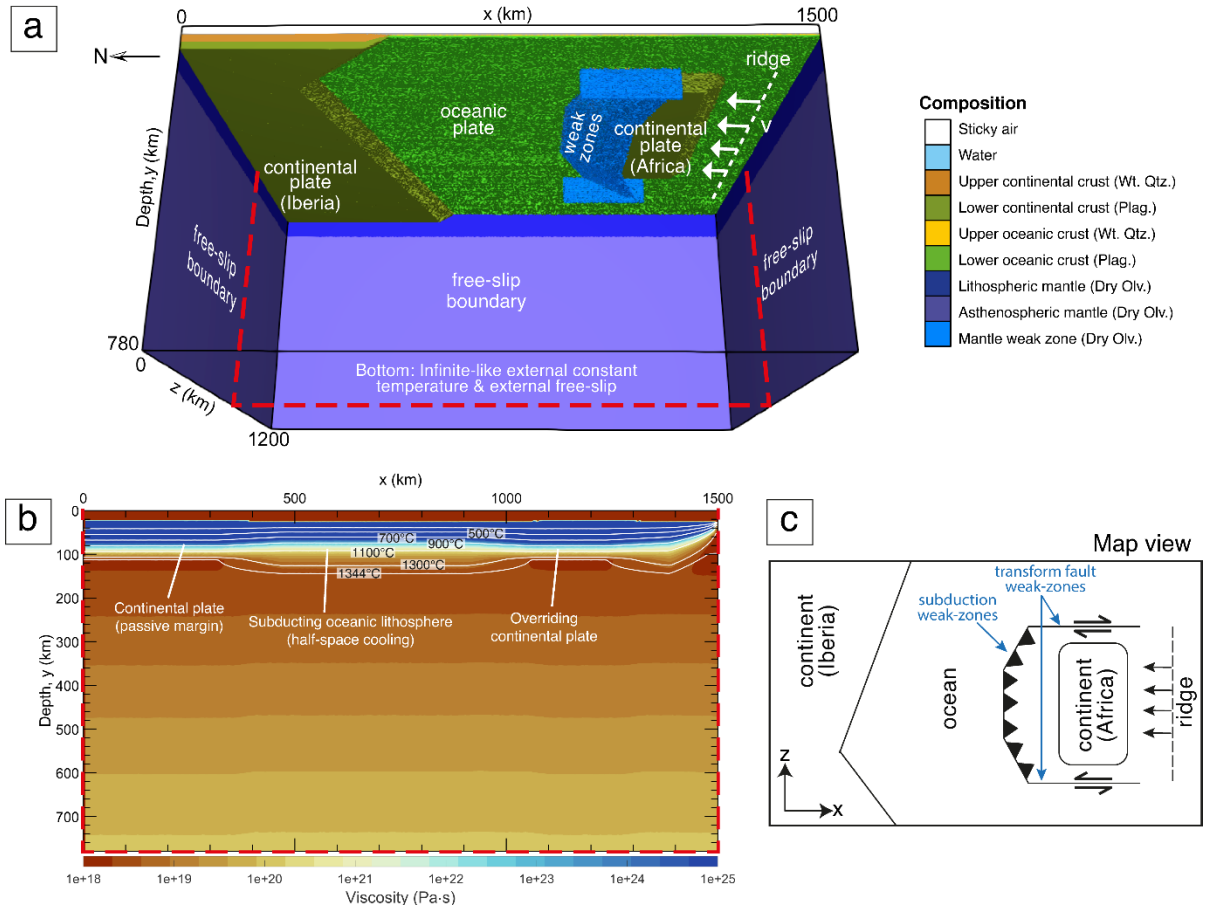

Fig 2. **Setup of Mod1-reference model**. a) 3D model domain (1500 × 780 × 1200 km) with colours representing different compositions. The flow law abbreviations are Wt Qtz. – wet quartzite; Plag. –Plagioclase; and Dry Olv. – Dry Olivine. Convergence is imposed by applying a uniform velocity (v) of 47 mm yr^{-1} until the slab reaches 200 km depth, after which v is either controlled by the sinking slab or reduced to another constant velocity. b) A cross-section profile of the viscosity. c) A map view of the model.

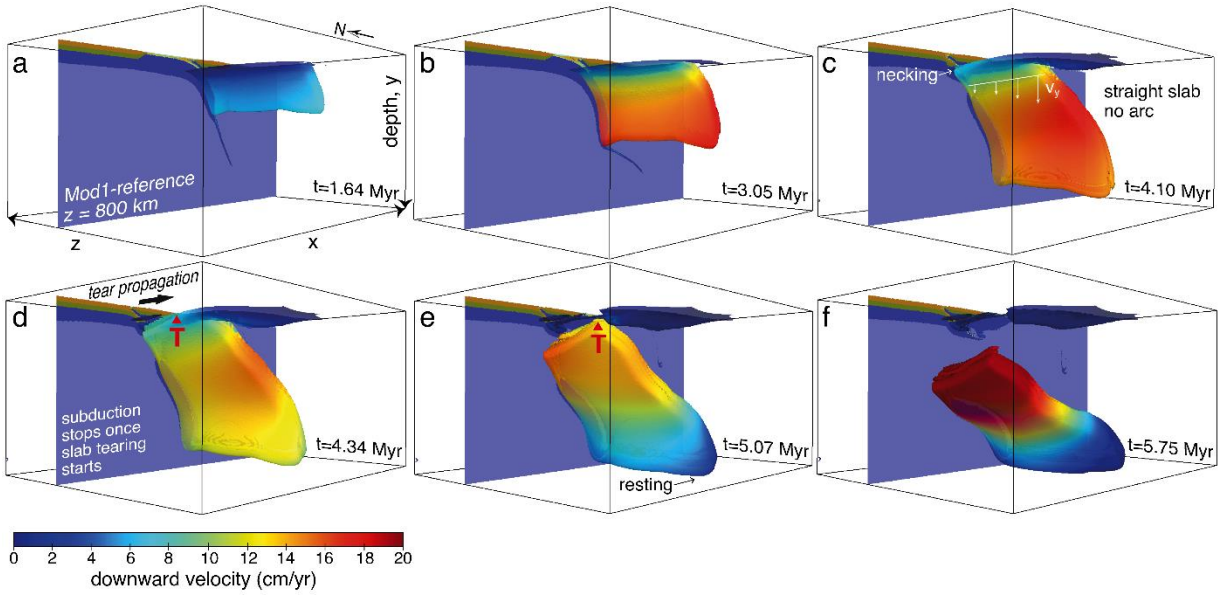

Fig 3. **The evolution of the slab's downward velocity (Mod1-reference)**. The slab structure shown here comes from the temperature isosurface, T=1300°C. The cross-section (z=800 km) shows the lithology/composition (for rock composition colour legends please refer to Fig 2. The red 'T' illustrates the position of the slab tear. Prior necking or slab tearing, the slab subducts with little lateral velocity variation across the slab (a and b). Once the necking and the tearing has started, the higher downward velocity now shifted to side of the slab that is still attached (c and d). After the slab is completely detached (f), the slab's downward velocity regained the lateral uniformity of downward velocity.

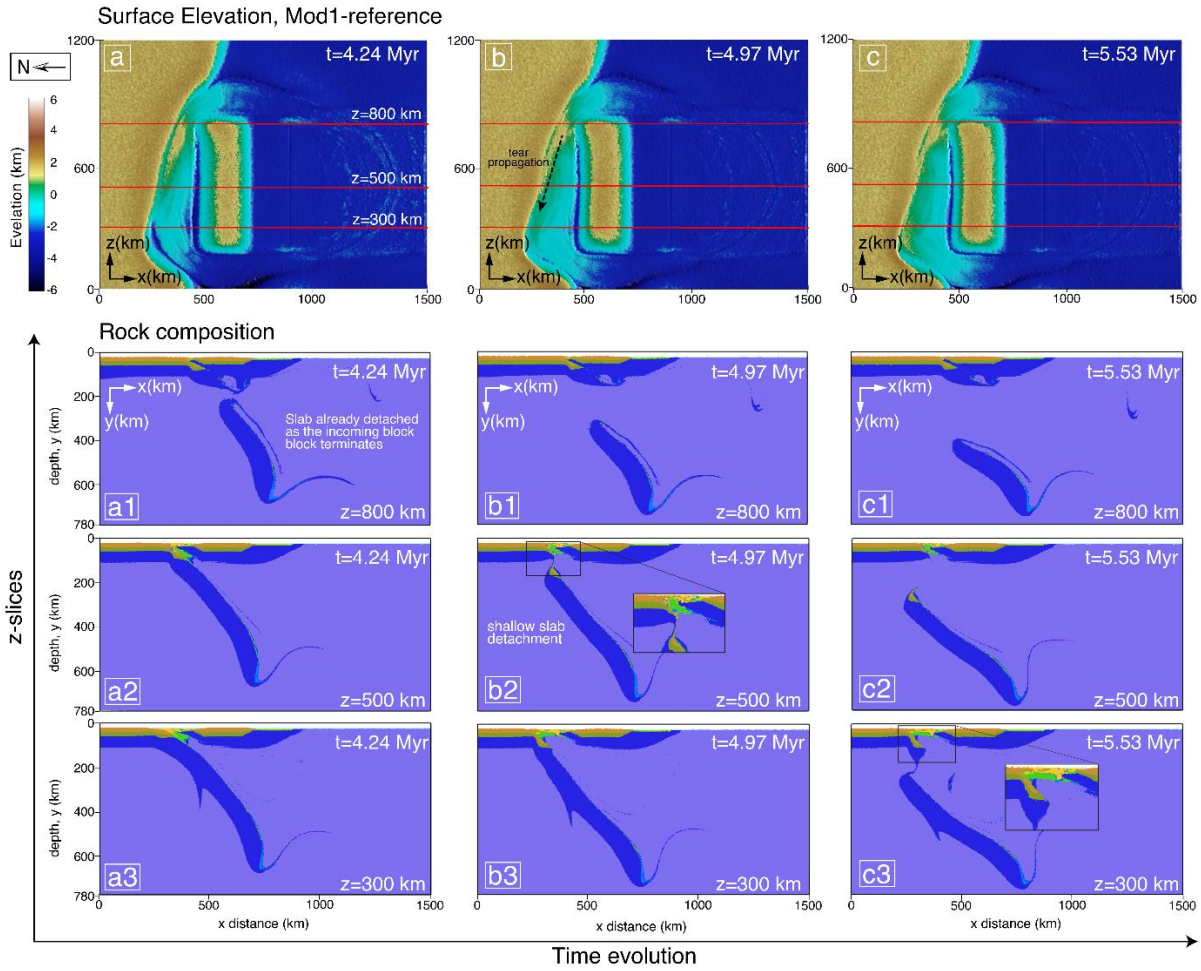

Fig 4. **Evolution of the reference model** (Mod1-reference) shown as surface topography (a, b, and c) and lithology (a1-3, b1-3, and c1-3). The colour coding for the lithology slices is the same as in Fig 2. Set (a) show the stage at which the continental-continental collision causes the incoming continental block to stop completely. The slab has already started to detach on the eastern side (z=800 km) by this point. In Set (b), the slab is half-torn with the attached portion of the slab still exerting slab-pull force. In Set (c), the tearing is approaching the western most side of the slab. Here the tearing/pinching occur at a deeper depth as the slab was still sinking until the arrival of the tearing. The tearing propagates westward as exhibited in a1, b2, and c3 cross-sections.

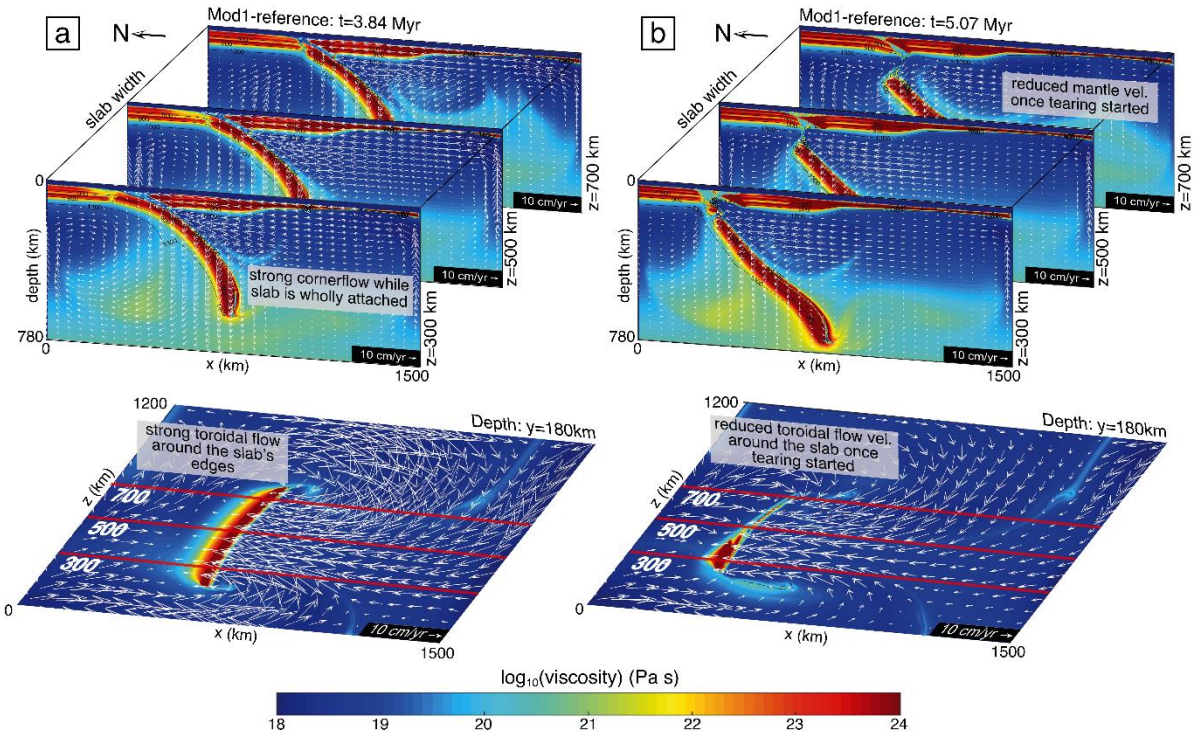

Fig 5 **Reference model viscosity cross-sections with velocity fields**. The upper panels shows the x-y cross-sections from z=300, 500, and 700 km, while the bottom panels shows the x-z cross-sections from the depth y=180 km, and the red lines correspond to the x-y slices in the panel above. The cross-sections in (a) come from a stage when the lithospheric slab is still wholly attached. The large hanging slab disturbs the mantle flow and causes mantle corner flow to build up, as well as causing strong mantle flow around the slab. The cross-sections in (b) are from the stage after slab tearing has started (on the eastern side). The mantle flow velocity is reduced as the slab-tear window allows the mantle to flow through.

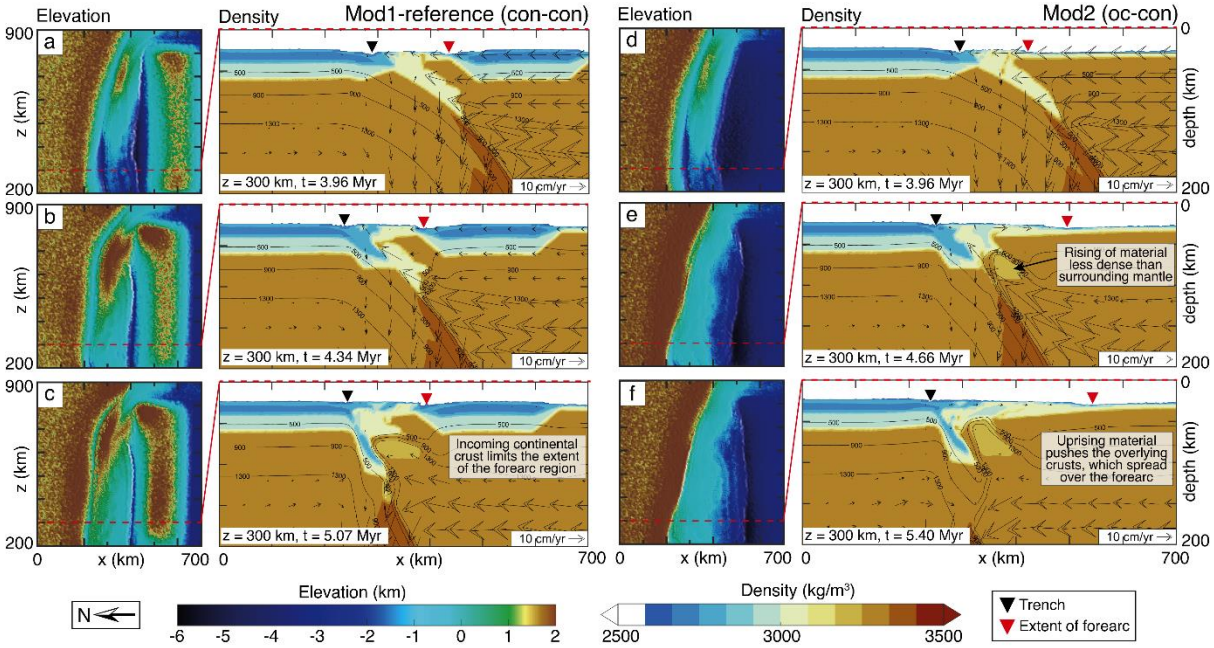

Fig 6 **The incoming continental crust limits the extent of forearc**. Shown here are elevation and density plots of model Mod1-reference (a, b, c) and Mod2 (d, e, f). The density cross-sections are taken from z = 300 km, shown as a red dashed line on each corresponding elevation plot. The black triangle indicates the position of the trench and the red triangle indicates the extent of the forearc. In both models, a body of less density (3200 kg/m^3) than the surrounding mantle exhumes up the subduction channel (c, e, f). The exhumed material thrusts under the overlying crust leading to a raised elevation. In Mod1-reference, the buoyant incoming continental crust (right, southern side of the model) limits the extent of the forearc region to the area in-between the passive margin and the incoming continental crust. In Mod2, the lack of a buoyant continental crust allows the crustal material, which are pushed up by mantle exhumation, to spread over a wider area and extending the forearc region.

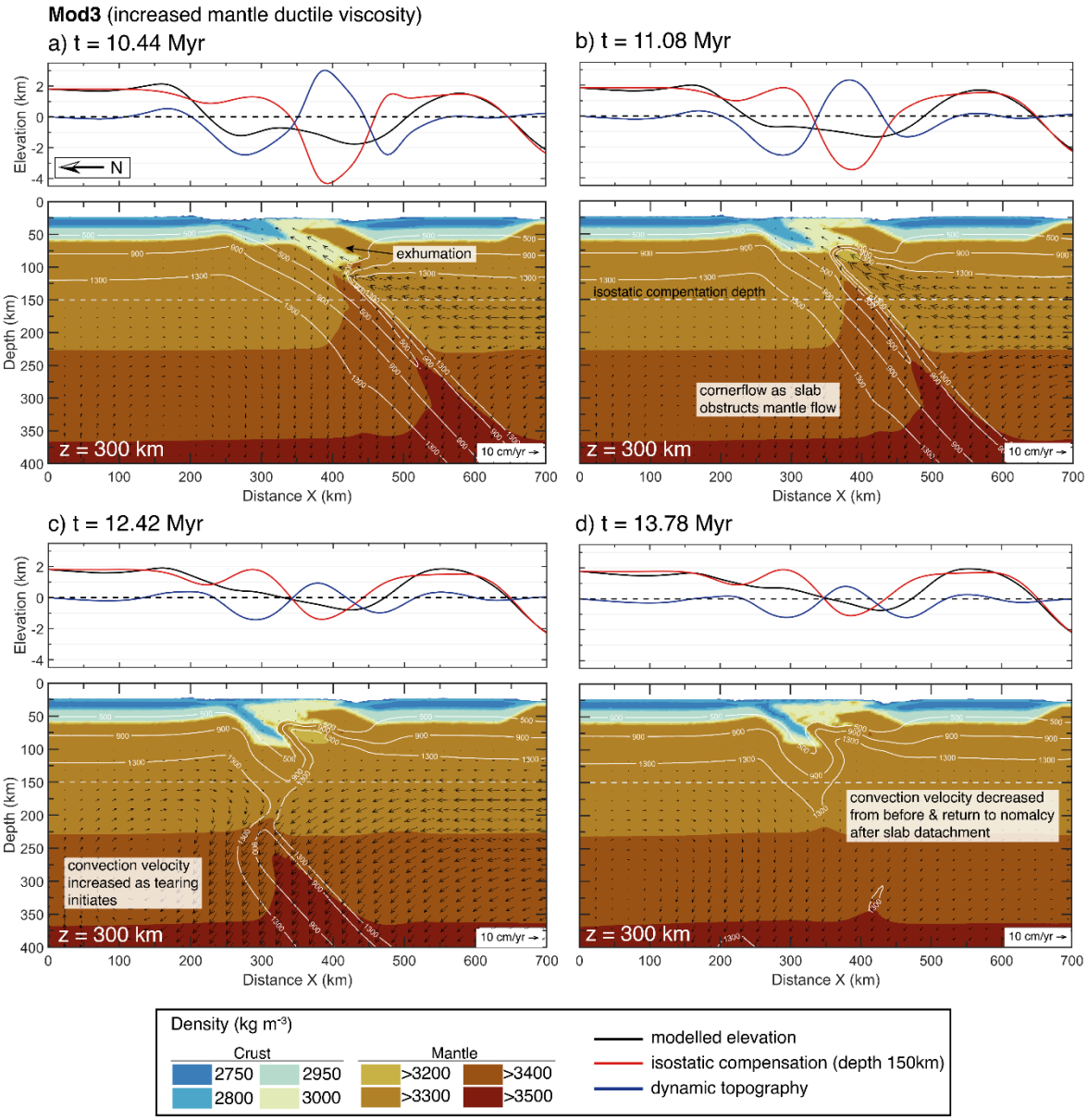

Fig 7. **Dynamic topography and density for model Mod3 (higher ductile viscosity of the mantle)**. The elevation plots (top panels) consist of: (i) total elevation resulting from the model (black); (ii) component of elevation corresponding to isostatic compensation of the crust (red); and (iii) component related to dynamic topography (blue). The isostatic effect was calculated with a compensation depth of 150 km (~128 km below crustal surface). The density (kg/m^3) distribution (bottom panels) is overlaid with temperature contours of the lithospheric mantle (500°C, 900°C, and 1300°C). (a) From the stage when the incoming continental block came to a complete stop. (b) Pre-detachment stage with ongoing exhumation of the subducted oceanic crust and corner flow as the slab obstructs mantle flow. (c) During necking and tearing when mantle flow focus on the detaching slab and decrease the convection velocity in the upper part of the mantle. (d) Post-detachment stage when the mantle flow returns to its unperturbed state and convection velocity are reduced (the detached slab is at 450–660 km depth).

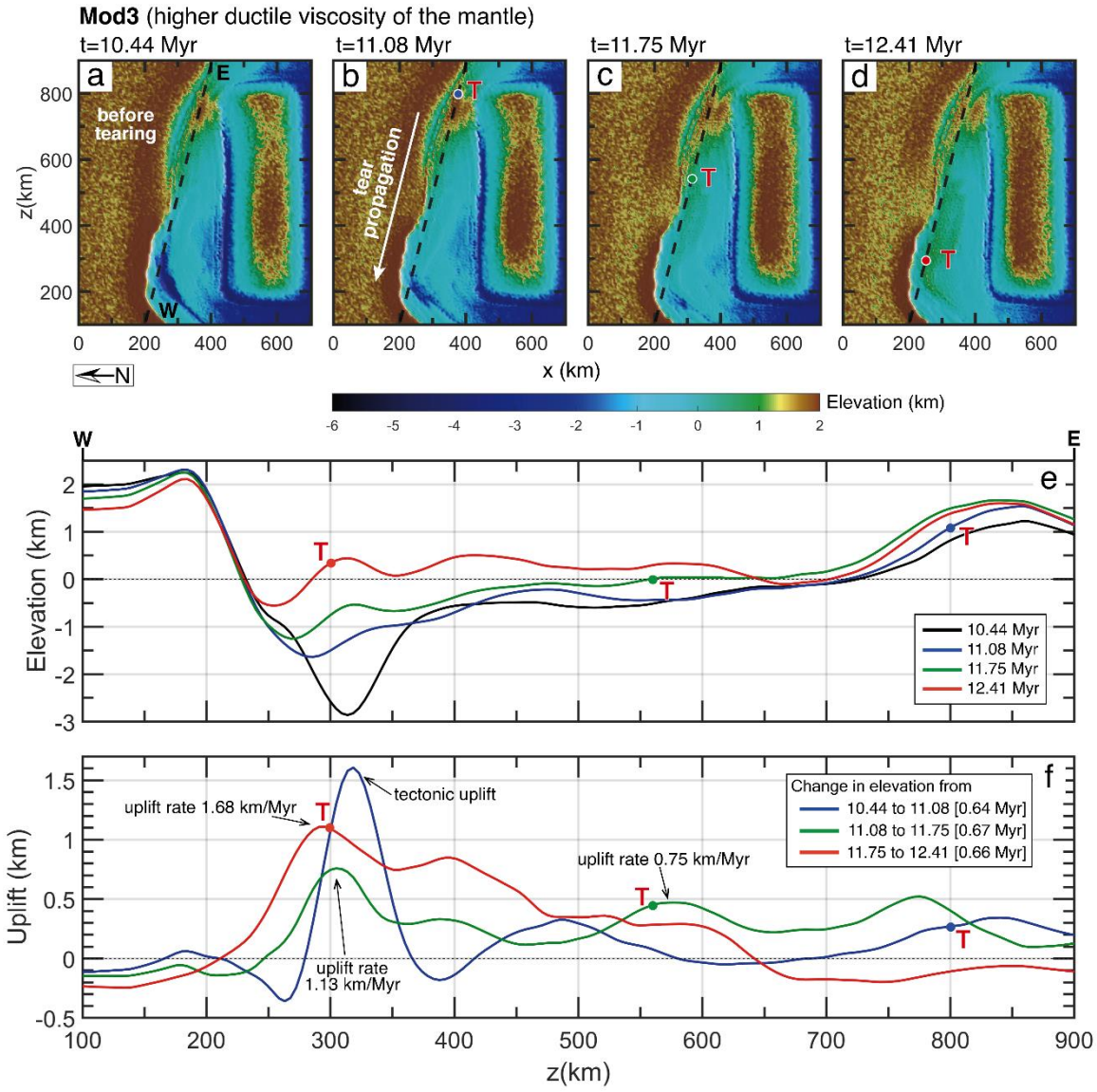

Fig 8. **Elevation evolution of model Mod3 (higher ductile viscosity of the mantle)**. (a), (b), (c), and (d) are map views of the model's surface elevation evolution with the tear propagating westward. The red 'T' indicates the slab-tear position in the subsurface. The dash lines (W-E) in (a) through (d) represent the elevation profiles shown in plot (e). Plot (f) shows the amount of uplift between time steps as the tearing propagates westward. The elevation increases as the tear propagates, with the maximum uplift rate of 1.68 km/Myr in the west. As the tear moves westward, the region toward the east of the profile W-E starts to subside, as shown with the red line in plot (e).

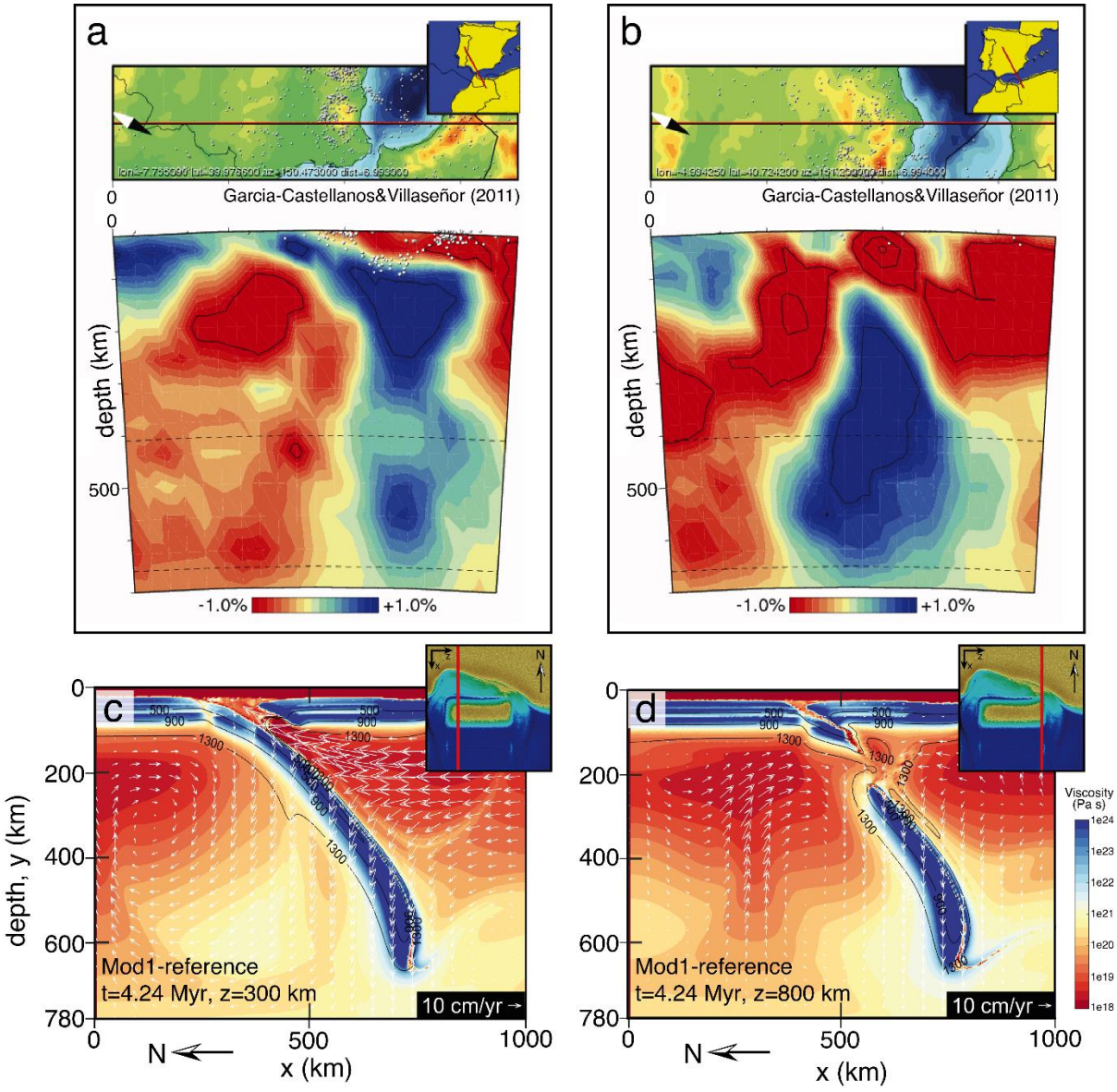

Fig 9. **Comparison of slab structure from Mod1-reference with the seismic tomography of the Western Mediterranean**. (a) and (b) are seismic tomographic images from Garcia-Castellanos & Villaseñor (2011) showing the distribution of fast- (blue) and slow-seismic-velocity (red). (c) and (d) are viscosity cross-sections from model Mod1-reference with (c) sliced from z=300 km, where the subducting slab is still attached and (d) sliced from z=800 km, where the slab has just started tearing. The subsets in (c) and (d) show the plan-view (x-z) of the surface elevation, and the red lines indicate the position of the corresponding cross-sections. The cross-sections from Mod1-reference resemble, to an extent, the seismic tomography from the Western Mediterranean, with the attached portion of the slab on the NW side (a) and the detached slab toward the NE side (b).